Hindawi Publishing Corporation
Mathematical Problems in Engineering
Volume 2014, Article ID 591807, 13 pages
http://dx.doi.org/10.1155/2014/591807

Research Article

Direct Numerical Simulation of Flow around a Circular Cylinder Controlled Using Plasma Actuators

Taichi Igarashi, Hiroshi Naito, and Koji Fukagata

Department of Mechanical Engineering, Keio University, Hiyoshi 3-14-1, Kohoku-ku, Yokohama 223-8522, Japan

Correspondence should be addressed to Koji Fukagata; fukagata@mech.keio.ac.jp

Received 27 December 2013; Accepted 29 May 2014; Published 22 June 2014

Academic Editor: Yonghong Wu

Flow around a circular cylinder controlled using plasma actuators is investigated by means of direct numerical simulation (DNS). The Reynolds number based on the freestream velocity and the cylinder diameter is set at $\mathrm{Re}_D = 1000$. The plasma actuators are placed at ±90° from the front stagnation point. Two types of forcing, that is, two-dimensional forcing and three-dimensional forcing, are examined and the effects of the forcing amplitude and the arrangement of plasma actuators are studied. The simulation results suggest that the two-dimensional forcing is primarily effective in drag reduction. When the forcing amplitude is higher, the mean drag and the lift fluctuations are suppressed more significantly. In contrast, the three-dimensional forcing is found to be quite effective in reduction of the lift fluctuations too. This is mainly due to a desynchronization of vortex shedding. Although the drag reduction rate of the three-dimensional forcing is slightly lower than that of the two-dimensional forcing, considering the power required for the forcing, the three-dimensional forcing is about twice more efficient.

1. Introduction

Flow around a bluff body causes a significant amount of drag. In addition, the vortices shed from the bluff body cause flow-induced noise; the resulting lift fluctuations may damage instruments. Therefore, significant efforts have been made to control the flow around a bluff body (see, e.g., Choi et al. [1]).

Flow control methods can be classified into passive and active ones. As the passive control methods, a splitter plate [2], dimples [3], tabs [4], and wavy surfaces [5] have been used, to name a few. For the active control methods, different types of actuators have been developed, as reviewed, for example, by Cattafesta and Sheplak [6]. As an example of active control of flow around a bluff body, Kim and Choi [7] performed a numerical simulation of a flow around a circular cylinder at $\mathrm{Re}_D = U_\infty D/\nu = 100 - 3900$ (where D, U_∞, and ν denote the cylinder diameter, the freestream velocity, and the kinematic viscosity, resp.) controlled by using blowing and suction and attained more than 20% drag reduction.

Recently, plasma actuators have attracted considerable attentions as novel devices for active control. The widely used single-dielectric barrier discharge (SDBD) plasma actuator is composed of two electrodes and a dielectric layer between them, as shown in Figure 1. A high frequency alternating-current (AC) voltage produces plasma between these electrodes. The charged particles are accelerated through the electric field and subsequently collide with neutral particles to generate a body force and induce a wall-jet-like flow. The plasma actuator has advantages in its light weight and no moving mechanical part; therefore, it is expected to be used in a wide range of applications. For more details on the physics and the applications of SDBD plasma actuators, readers are referred to the excellent review papers by Roth and Dai [8] and Corke et al. [9].

Grundmann et al. [10] experimentally and numerically investigated the effect of plasma actuator applied to a boundary layer separation control and verified its effectiveness. Cho and Shyy [11] considered an airfoil with a plasma actuator and investigated the effect of both open-loop and closed-loop controls. In these previous studies, the so-called two-dimensional forcing was used. In the two-dimensional forcing, the body force by the plasma actuator is directed in the streamwise direction and its magnitude is uniform in the spanwise direction, so that the body force delays the flow

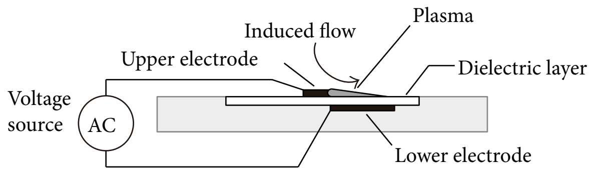

Figure 1: Structure of an SDBD plasma actuator (redrawn based on Corke et al. [9]).

separation by directly adding a mean momentum into the boundary layer.

In contrast, the so-called three-dimensional forcing has also been studied. In the three-dimensional forcing, the magnitude of body force varies in the spanwise direction or the body force vectors are directed in the spanwise direction, so that three-dimensional flow structure is induced to destroy the two-dimensional vortices. Kozlov and Thomas [12] experimentally investigated a flow around a circular cylinder at a high Reynolds number ($\mathrm{Re}_D = 85,000$) controlled using plasma actuators. They considered not only two-dimensional forcing but also three-dimensional forcing. In their three-dimensional forcing, the plasma actuators are placed in the circumferential direction and the flow is induced in the spanwise direction. Bhattacharya and Gregory [13] experimentally examined three-dimensional forcing at $\mathrm{Re}_D = 4700$. In their three-dimensional forcing, the plasma actuators inducing streamwise flows are placed on a circular cylinder periodically in the spanwise direction with the wavelength of $\lambda = 4D$. In both studies, a better drag reduction effect than that by two-dimensional forcing was obtained.

Despite the studies introduced above, there have been fewer studies on the flow around a circular cylinder controlled using the three-dimensional forcing of plasma actuators. Detailed effects of the forcing amplitude of the two-dimensional and three-dimensional forcings on the flow modifications are still to be investigated. Therefore, in the present study, we investigate the flow around a circular cylinder controlled using plasma actuators by means of direct numerical simulation (DNS). We consider both the two-dimensional forcing and the three-dimensional forcing and investigate the effect of forcing amplitudes on the flow modifications.

2. Numerical Methods

2.1. Direct Numerical Simulation. We consider a circular cylinder in an incompressible uniform flow. The Reynolds number is $\mathrm{Re}_D = 1000$. This Reynolds number is chosen so that a direct numerical simulation (DNS) can be performed, since no turbulence models have been validated for a flow controlled using plasma actuators. The governing equations are the continuity and the Navier-Stokes equations; that is,

$$\nabla \cdot \vec{u} = 0,$$
$$\frac{\partial \vec{u}}{\partial t} + \nabla \cdot (\vec{u}\vec{u}) = -\nabla p + \frac{1}{\mathrm{Re}_D}\nabla^2 \vec{u} + \vec{f}, \tag{1}$$

where $\vec{u}$ and p are the velocity and the pressure, respectively, and $\vec{f}$ denotes the body force induced by the plasma actuators described later. All the quantities are made dimensionless by using the fluid density, ρ, the freestream velocity, U_∞, and the cylinder diameter, D.

The present simulations are performed by using the DNS code of Naito and Fukagata [14]. The governing equations are spatially discretized in the cylindrical coordinates by using the energy conservative second-order accurate finite difference method [16] and temporally integrated by using the low-storage third-order Runge-Kutta/Crank-Nicolson (RK3/CN) scheme [17, 18] with an SMAC-like pressure correction [19]. The pressure Poisson equation is solved by using the fast Fourier transform (FFT) in the azimuthal (θ) and the spanwise (z) directions and the tridiagonal matrix algorithm (TDMA) in the radial (r) direction.

The computational grid is shown in Figure 2. The size of computational domain (L_r, L_z), the number of computational cells (N_r, N_θ, and N_z), and the size of a computational cell ($\Delta r_{\min}$, Δz) are summarized in Table 1. The computational grid is nonuniform in the radial (r) direction and uniform in θ and z directions. The size of the computational domain is $70D$ to minimize the influence from the boundaries.

A uniform velocity $U_\infty = 1$ is imposed at the inlet boundary ($|\theta| \leq (3/4)\pi$, where θ denotes the angle from the front stagnation point) and the convective velocity condition, that is,

$$\frac{\partial \vec{u}}{\partial t} + U_\infty \frac{\partial \vec{u}}{\partial x} = 0, \tag{2}$$

is used at the outlet boundary ($|\theta| > (3/4)\pi$). The periodic boundary condition is applied in z direction. On the surface of the circular cylinder, the no-slip condition is applied and the pressure gradient is set to be zero.

Verification and validation for the base flow (i.e., without plasma actuators) have been reported in Naito and Fukagata [14]. The computational cell has been confirmed to be sufficiently small to obtain the statistical data; for instance, change in the mean drag coefficient was less than 1% when twice finer Δz was used. Good agreement with the data available in literature has been obtained on the mean drag coefficient, root mean square (RMS) of the lift coefficient, the Strouhal number, and the base pressure coefficient. For more details, the readers are referred to Naito and Fukagata [14].

2.2. Body Force by Plasma Actuator. The electric field formed around the electrodes is a consequence of very complex ion transport phenomena. Therefore, if one is interested in temporal variations of the body force field, the detailed ion transport should be solved. In contrast, if one is interested in the effect of body force on a relatively low-speed fluid flow, such as the present study, it is more efficient to use a time-averaged model because the frequency of the imposed AC voltage signal is much higher than that of flow. For instance, an air flow at $U_\infty = 1.5$ m/s on a $d = 1 \times 10^{-2}$ m cylinder results in $\mathrm{Re}_D = 1000$ and the vortex shedding frequency of 30 Hz, while the frequency of imposed AC voltage signal is of the order of 10 kHz. Yamamoto and Fukagata [20],

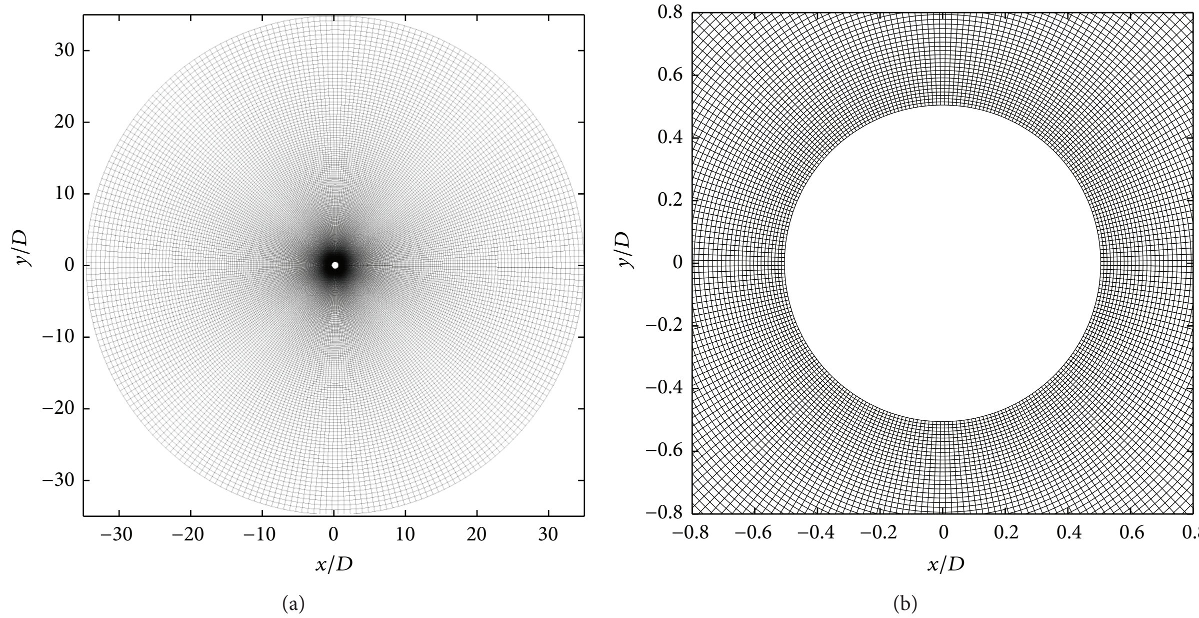

FIGURE 2: Computational grid: (a) overview; (b) zoom-up view near the cylinder (from Naito and Fukagata [14]).

TABLE 1: The size of computational domain (L_r, L_z), the number of computational cells (N_r, N_θ, and N_z), and the size of a computational cell.

L_r/D	L_z/D	N_r	N_θ	N_z	$\Delta r_{\min}/D$	$\Delta z/D$
70	2	220	256	32	1.00×10^{-2}	6.25×10^{-2}

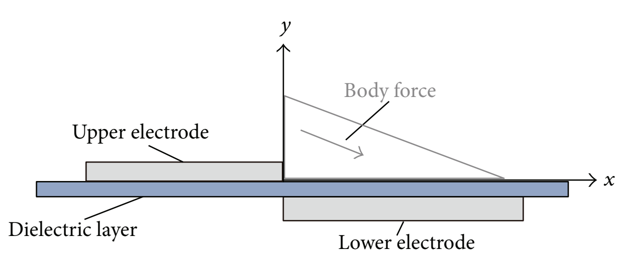

FIGURE 3: Shyy's model (redrawn based on Shyy et al. [15]).

who performed detailed numerical simulations of the ion transports in a plasma actuator, demonstrated that a time-averaged body force field can reasonably be used when the typical frequency of flow is less than 30 times of that of the voltage signal.

As a time-averaged model, we use Shyy's model (Shyy et al. [15]), as shown in Figure 3. This model assumes a linear decay of the electric field, $E(x, y)$, with its maximum at the point of the shortest distance between the electrodes, which can be expressed by

$$E(x, y) = \left|\vec{E}\right| = E_0 - k_1 x - k_2 y, \tag{3}$$

where E_0 is the maximum electric field strength with k_1 and k_2 being positive constants. Here, the values proposed by Shyy et al. [15], that is, $E_0 = 226.27\,\text{kV/cm}$, $k_1 = 6.54 \times 10^2\,\text{kV/cm}^2$, and $k_2 = 13.08 \times 10^2\,\text{kV/cm}^2$, are used. The electric field vector is assumed to be unidirectional and its components E_x and E_y are modeled as

$$E_x = \frac{k_2}{\sqrt{k_1^2 + k_2^2}}\left|\vec{E}\right|, \qquad E_y = -\frac{k_1}{\sqrt{k_1^2 + k_2^2}}\left|\vec{E}\right|. \tag{4}$$

The time-averaged body force, $\vec{f}$, is computed as

$$\vec{f} = \vartheta \alpha \rho_c e_c \vec{E} \Delta t, \tag{5}$$

where $e_c = 1.60 \times 10^{-19}$ C is the elementary charge, ϑ (the frequency of the applied voltage signal), Δt (the discharge time), and ρ_c (the charge number density) are the parameters depending on the operating condition, and α is the collision efficiency assumed to be unity. By representing these model constants altogether by a single parameter, c, the magnitude of the body force can be expressed as

$$f(x, y) = \left|\vec{f}\right| = c\left(E_0 - k_1 x - k_2 y\right). \tag{6}$$

Table 2: Forcing amplitude of plasma actuators.

Value of k_3	Notation
0.0	No control (NC)
0.1, 0.2, 0.4, 0.6	Lower forcing amplitude
0.8	The amplitude inducing a velocity similar to that in the experiment [21]
1.0, 1.2	Higher forcing amplitude

The purpose of the present study is to investigate the effect of forcing amplitude on the flow modification. Therefore, we set the parameter c as

$$c = \left(1 \times 10^{-4}\ \mathrm{C/cm^3}\right) \times k_3. \tag{7}$$

The forcing amplitude is varied by k_3 from 0.0 to 1.2, as shown in Table 2. The resultant induced velocity will be shown in Section 3 as a function of k_3.

We examine four types of arrangement as shown in Figure 4. The uncontrolled flow (i.e., base flow) is denoted as Case NC; Case 1 is a two-dimensional forcing; Cases 2 and 3 are three-dimensional forcings. In all cases, the plasma actuators are placed at ±90° from the front stagnation point.

3. Results and Discussion

3.1. Two-Dimensional Forcing. Figure 5 shows the maximum mean streamwise velocity around a plasma actuator, $U_{\max}$, as a function of the forcing amplitude, k_3. The velocity is found to increase monotonically as the amplitude parameter k_3 increases. In the figure, the results from four different simulations, Cases 1a–1d, corresponding to four different time instants when the plasma actuators are turned on, are presented, because it is found from the results that the resultant values of $\overline{C_D}$ and C_L' (shown below) are slightly dependent on the turn-on time.

The dependency on the turn-on time is likely to be due to the low frequency variation of lift fluctuations. Figure 6 shows the time traces of the drag coefficient, C_D, and the lift coefficient, C_L, defined, respectively, as

$$C_D = \frac{F_D}{(1/2)\,\rho U_\infty^2 D L_z}, \qquad C_L = \frac{F_L}{(1/2)\,\rho U_\infty^2 D L_z}, \tag{8}$$

where F_D and F_L denote the drag and the lift forces. In addition to the high frequency fluctuations corresponding to the vortex shedding ($T \simeq 5$), very low frequency fluctuations ($T \sim 100$) are observed.

The low frequency fluctuations can be explained by instantaneous vortical structures (identified by using the second invariant of deformation rate tensor) at two different time instants, as exemplified in Figure 8. At $t = 50$ (when the amplitude of lift fluctuations is small), fine streamwise vortices are populated in the wake and spanwise vortices are hardly seen in the far wake. On the other hand, at $t = 200$ (when the amplitude of lift fluctuations is large), spanwise vortices are pronounced in the far wake. Namely, the amplitude of lift fluctuations corresponds to the degree of two-dimensionality of the vortical structure.

Due to the low frequency fluctuations, the integration time should be set carefully in the computation of statistics. Figure 7 shows the mean drag, $\overline{C_D}$, and the root mean square (RMS) of lift fluctuations, C_L', as functions of the integration time, T. From this, we judge that $T = 500$ is sufficient as the integration time for accumulation of statistics.

Figures 9(a) and 9(b) show $\overline{C_D}$ and C_L' as functions of the forcing amplitude, k_3. The mean drag, $\overline{C_D}$, is found to monotonically decrease as the forcing amplitude increases; the maximum drag reduction rate is about 45% at $k_3 = 1.2$. On the other hand, C_L' exhibits complicated dependency on k_3; it is at a comparable level to that of Case NC up to $k_3 = 0.6$ and it significantly decreases for $k_3 > 0.6$. The relationship between $\overline{C_D}$ and C_L' is mapped in Figure 9(c). It is clearly observed that up to $k_3 = 0.6$ the drag is reduced, while the lift fluctuations are not much suppressed; for $k_3 > 0.6$, both the drag and the lift fluctuations are suppressed. From this, it is conjectured that there is a transition of flow characteristics around $k_3 = 0.6$.

The transition of flow characteristics is illustrated by the mean streamwise velocity near the surface (Figure 10) and instantaneous vortical structures (Figure 11). On the cylinder surface, separation is found to be delayed at all amplitudes. Moreover, separation looks more synchronized in the spanwise direction at higher amplitudes. In the wake, the vortical structure is considerably different between the cases of weaker forcing ($k_3 = 0.4$) and stronger forcing ($k_3 = 0.8$ and 1.2). The vortical structure at $k_3 = 0.4$ is not so much different from that of the uncontrolled flow. At $k_3 = 0.8$ and 1.2, while two-dimensionality of separation is enhanced, the shed vortices seem to be too weak to generate strong streamwise vortices in the far wake. From the observations above, two different mechanisms are considered to play in the modification of flow: one is the separation delay, which reduces the drag and the amplitude of shed vortices; the other is the spanwise synchronization of the vortex shedding, which raises the lift fluctuations. The change in C_L' suggests that these two effects compensate each other at $k_3 < 0.6$ and the former effect exceeds at $k_3 > 0.6$.

Figure 12 shows the distributions of pressure coefficient on the cylinder surface, C_p, as functions of the angle from the stagnation point, θ, defined as

$$C_p = \frac{\overline{p_w} - p_\infty}{(1/2)\,\rho U_\infty^2}, \tag{9}$$

where $\overline{p_w}$ and p_∞ denote the mean wall pressure and the freestream pressure, respectively. The effect of plasma actuator is similar at all amplitudes, although there is a difference in its magnitude. In $30^\circ < \theta < 90^\circ$, the pressure decreases due to the acceleration by the plasma actuator; at $\theta = 90^\circ$, the pressure rapidly recovers by gaining momentum from the plasma actuator; around $\theta = 100^\circ$, the pressure

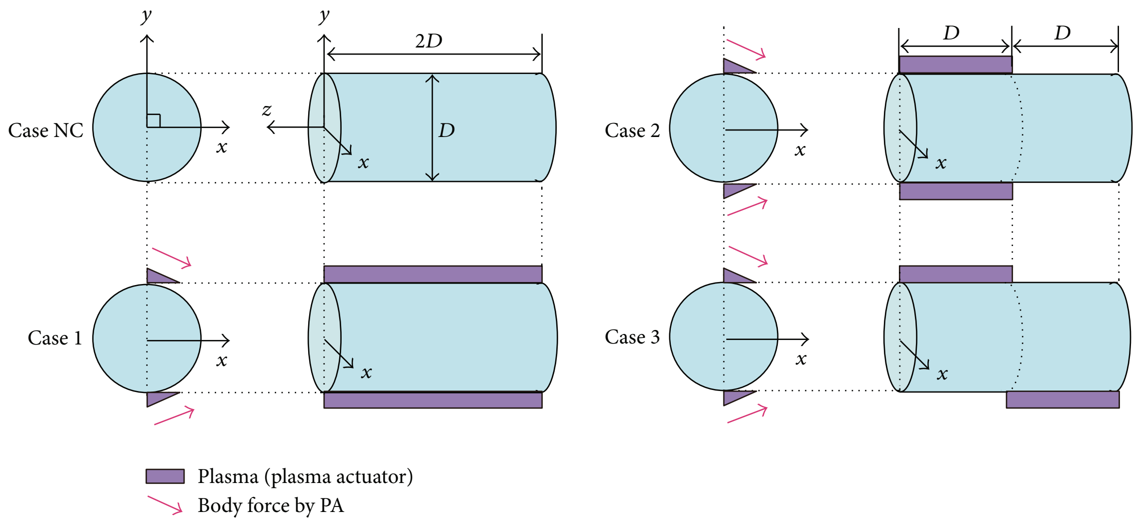

FIGURE 4: Arrangement of plasma actuators.

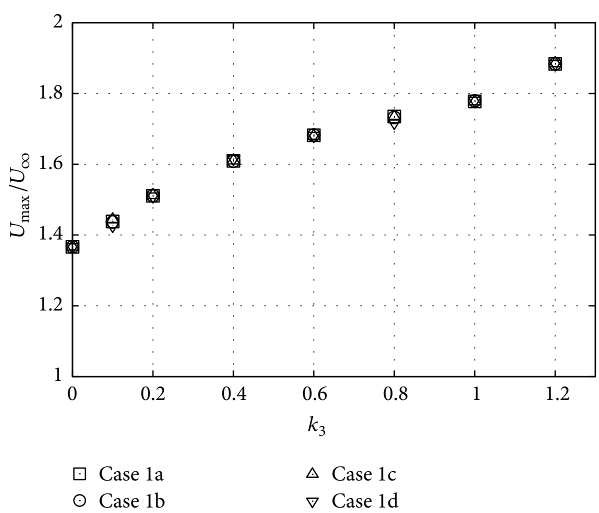

FIGURE 5: Maximum velocity of induced flow by the plasma actuator for different forcing amplitudes (k_3) in Case 1.

gradient reverses with flow separation; and finally on the rear surface the pressure recovers again with a larger value than that in Case NC. From the definition of drag, the greater recovery on the rear surface is most responsible for the drag reduction.

On the other hand, the change in C_L' can be explained by the RMS pressure coefficient, C_p', defined as

$$C_p' = \frac{\sqrt{\overline{p'^2}}}{(1/2)\,\rho U_\infty^2}, \tag{10}$$

as shown in Figure 13. The dependency of C_p' on k_3 is complicated. At $k_3 = 0.1$ and 0.2, C_p' decreases and the peak location moves backward. From $k_3 = 0.2$ to $k_3 = 0.4$, the maximum value is almost unchanged, but the peak location still moves backward. The peak value increases again at $k_3 = 0.6$ to the same level as that of Case NC; then C_p' significantly decreases for higher k_3 with the peak location nearly unchanged. This behavior is in accordance with the complicated dependency of C_L' on k_3 observed in Figure 9 and it can be explained by the two different effects discussed above: the suppression of vortex shedding amplitude and the two-dimensionalization of separation. In particular, the considerable reduction of C_L' at $k_3 > 0.6$ can be attributed to the suppression of C_p' on the entire surface.

3.2. Three-Dimensional Forcing. In the cases of three-dimensional forcing, the results are found to be independent of the initial flow conditions unlike the cases of two-dimensional forcing.

Figure 14 shows the maximum mean streamwise velocity around the upper plasma actuator in Case 2. Positions 1 and 2 denote the locations where the plasma actuator is present and absent, respectively. As k_3 increases, U_{max} at Position 1 is found to increase nearly monotonically; however, its magnitude is smaller than that in Case 1. In contrast, the velocity at Position 2 is less than that in Case NC. The difference in the mean streamwise velocity fields at Positions 1 and 2 is illustrated in Figure 15. While at Position 1 the separation is delayed similarly to the case of two-dimensional forcing (Figure 10(b)), and the velocity above the cylinder is lower than that in Case 1. The velocity at Position 1 is likely to be affected by the low velocity at Position 2.

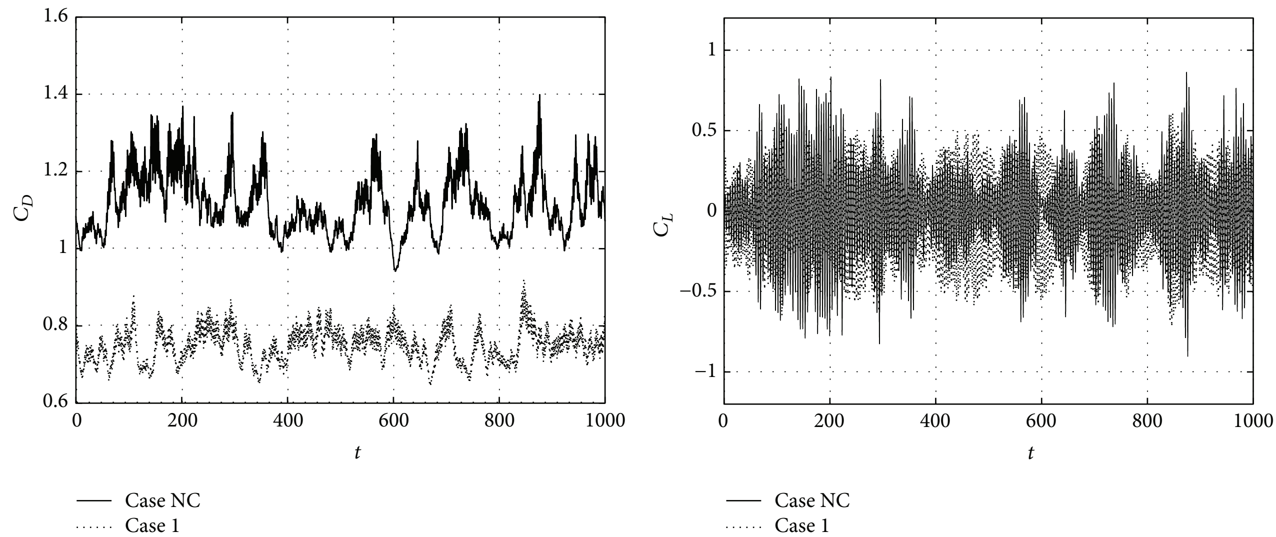

(a) (b)

Figure 6: Time traces in uncontrolled flow and Case 1 ($k_3 = 0.8$): (a) drag coefficient, C_D; (b) lift coefficient, C_L.

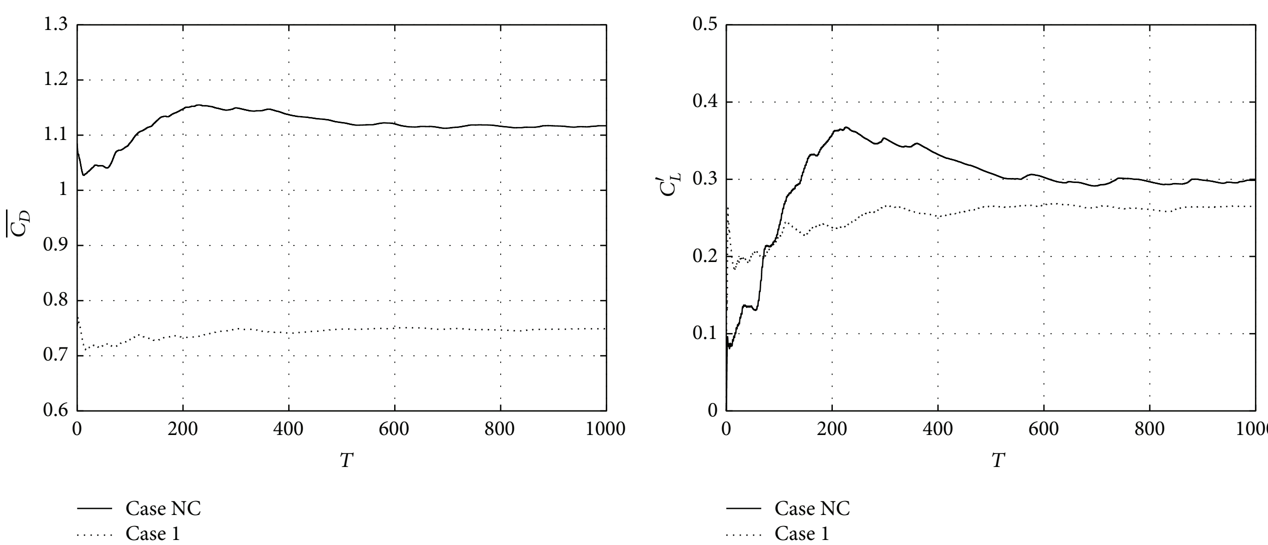

(a) (b)

Figure 7: Mean drag and RMS lift fluctuations computed using different integration time, T, in Case NC and Case 1 ($k_3 = 0.8$): (a) mean drag, $\overline{C_D}$; (b) RMS lift fluctuations, C_L'.

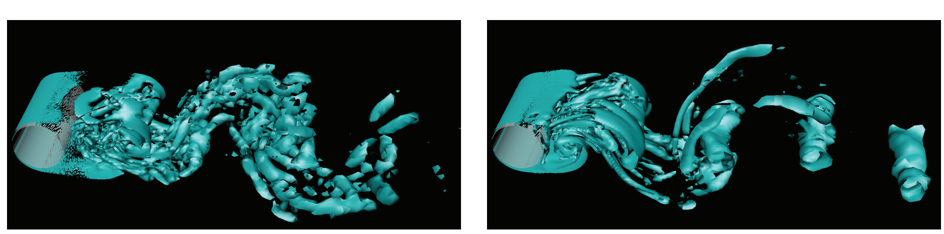

(a) (b)

Figure 8: Vortical structure in Case NC identified by isosurfaces of $\|\Omega\|^2 - \|S\|^2 = 1.0$: (a) $t = 50$; (b) $t = 200$.

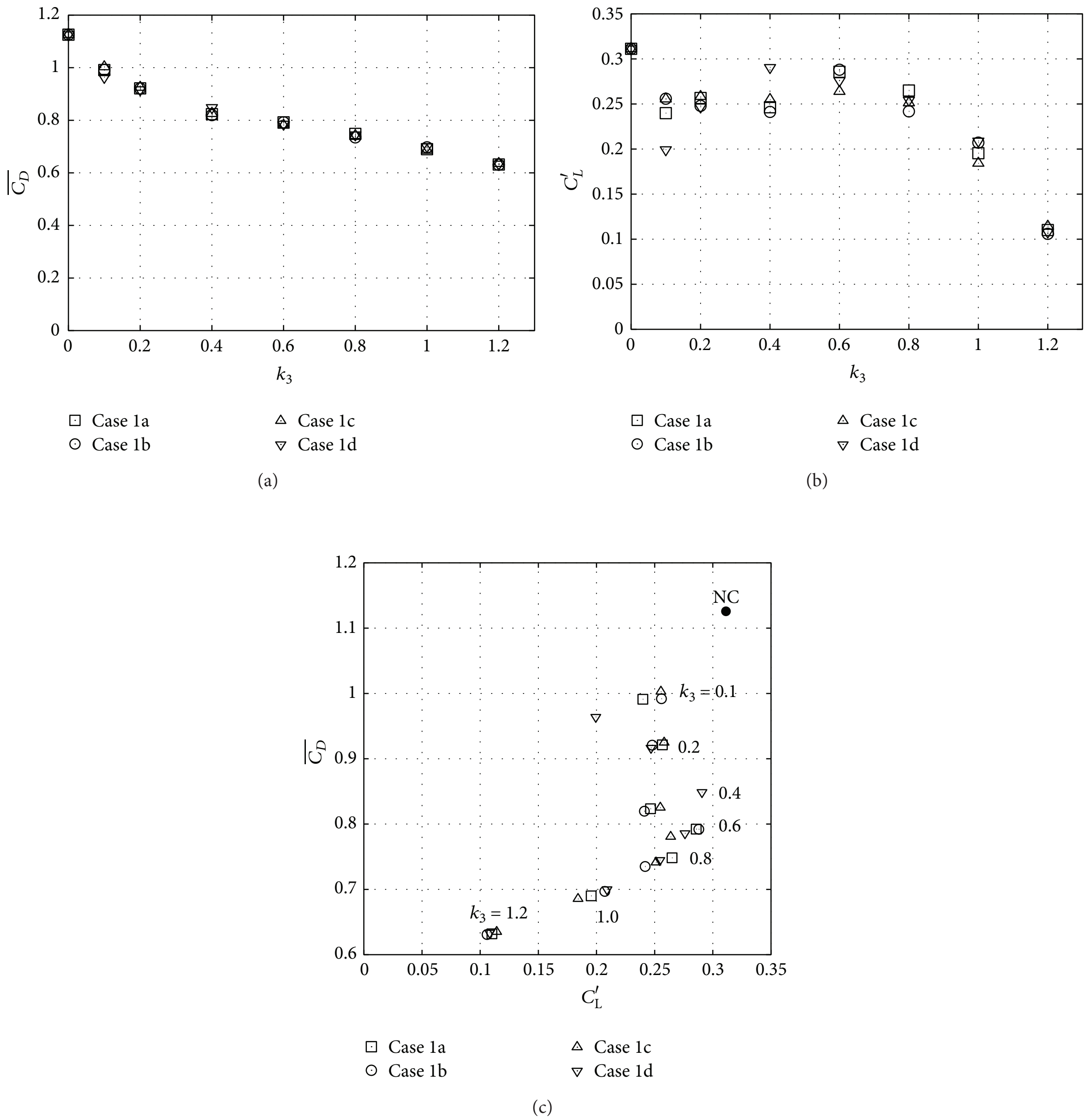

Figure 9: Mean drag and RMS lift fluctuations for different forcing amplitudes (k_3) in Case 1: (a) mean drag, $\overline{C_D}$; (b) RMS lift fluctuations, C_L'; (c) $\overline{C_D}$ versus C_L'.

Figure 16 shows instantaneous three-dimensional vortical structures. Vortices are observed to have completely been vanished in the near wake. The far wake is turbulent; however, no clear two-dimensional structure can be observed unlike Case NC and Case 1.

Figure 17 shows $\overline{C_D}$ and C_L' as functions of k_3. The dependency of $\overline{C_D}$ on k_3 in Cases 2 and 3 is similar to each other. Unlike the case of two-dimensional forcing, there is an optimum amplitude ($k_3 = 0.4$) at which $\overline{C_D}$ is minimized; the maximum drag reduction rate is about 34%. An excellent feature of the three-dimensional forcing appears in the lift fluctuation, C_L'; it is drastically suppressed in a wide range of k_3 due to three-dimensionalization of vortex shedding. The relationship between $\overline{C_D}$ and C_L' is mapped in Figure 18. In Cases 2 and 3, both the mean drag $\overline{C_D}$ and the lift fluctuations C_L' are decreased from those in Case NC. In particular, reduction in C_L' is much larger than that in Case 1 even at low forcing amplitudes. In both cases, the maximum reduction

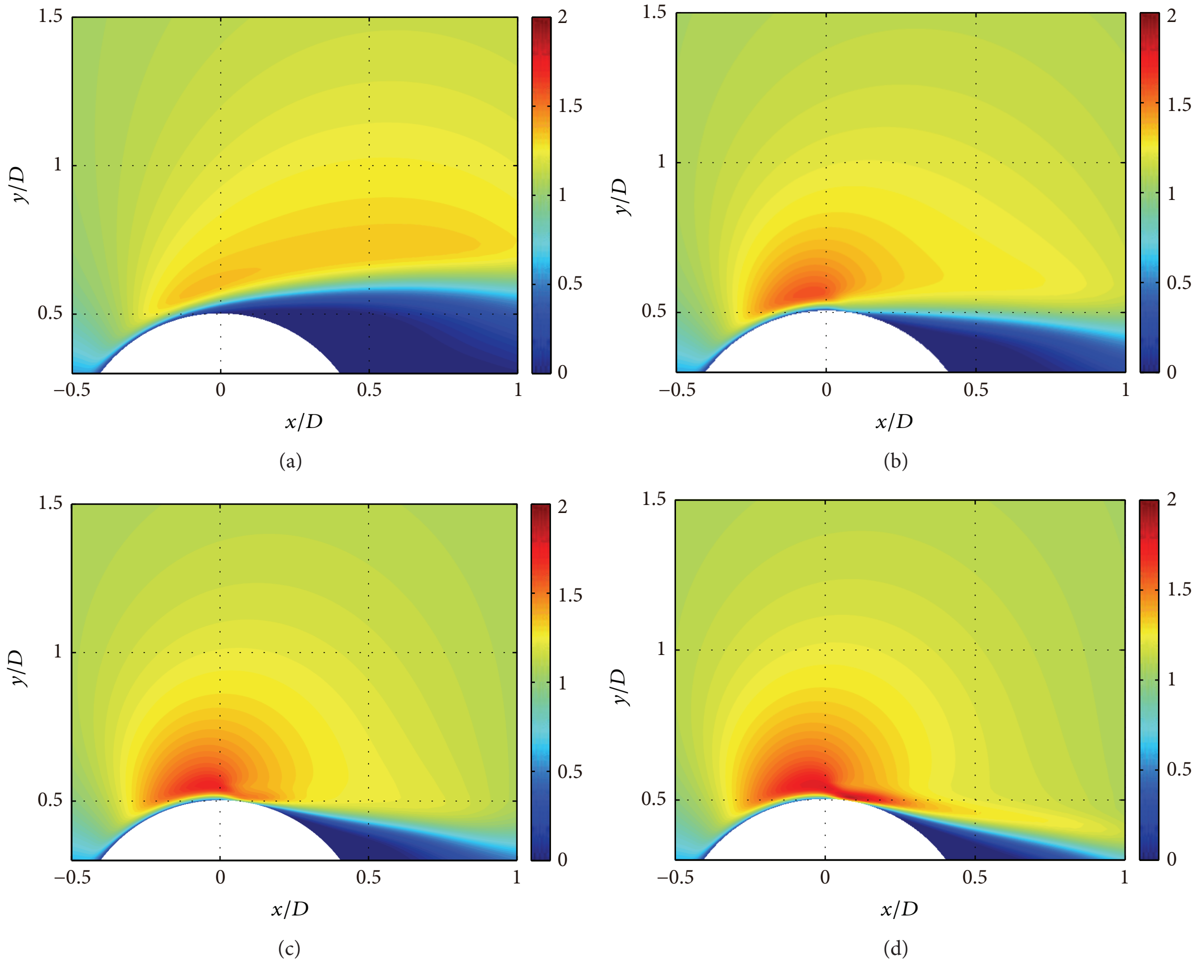

Figure 10: Mean streamwise velocity (U/U_∞) around the upper plasma actuator: (a) Case NC; (b) Case 1, $k_3 = 0.4$; (c) Case 1, $k_3 = 0.8$; (d) Case 1, $k_3 = 1.2$.

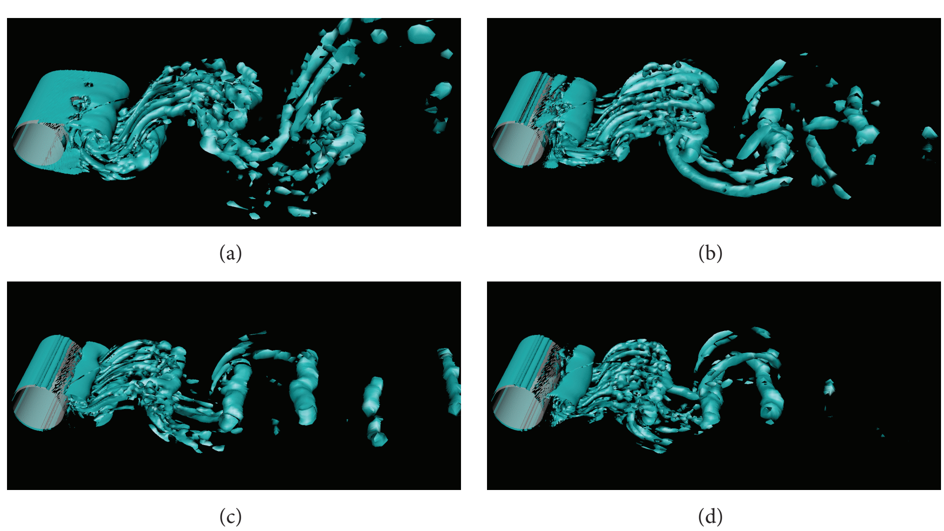

Figure 11: Instantaneous vortical structure identified by isosurfaces of $\|\Omega\|^2 - \|S\|^2 = 1.0$: (a) Case NC; (b) Case 1, $k_3 = 0.4$; (c) Case 1, $k_3 = 0.8$; (d) Case 1, $k_3 = 1.2$.

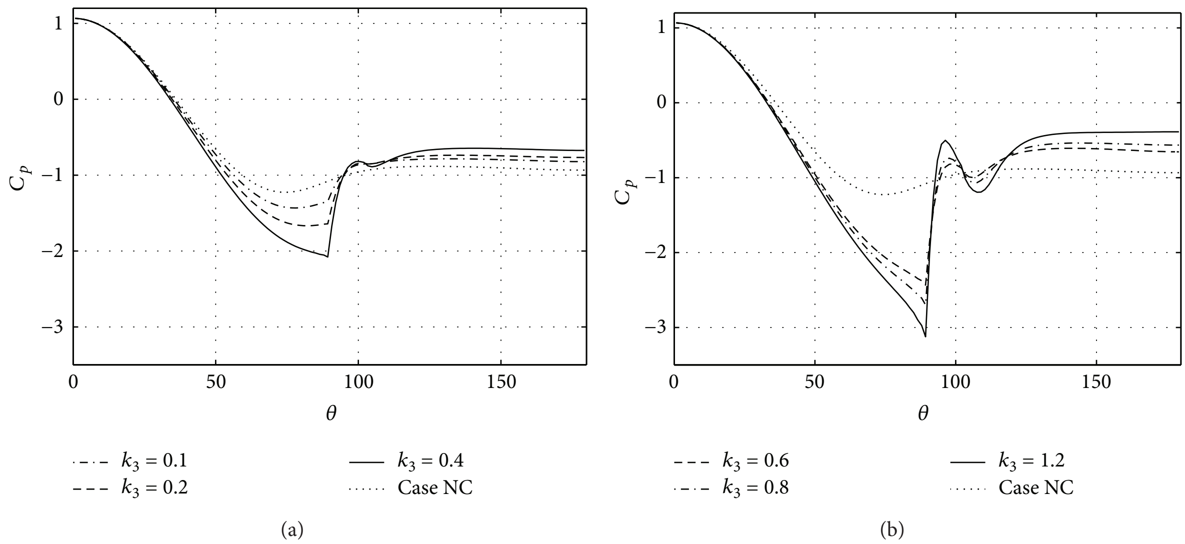

FIGURE 12: Pressure distribution on the cylinder surface in Case 1: (a) k_3 = 0.1, 0.2, and 0.4; (b) k_3 = 0.6, 0.8, and 1.2.

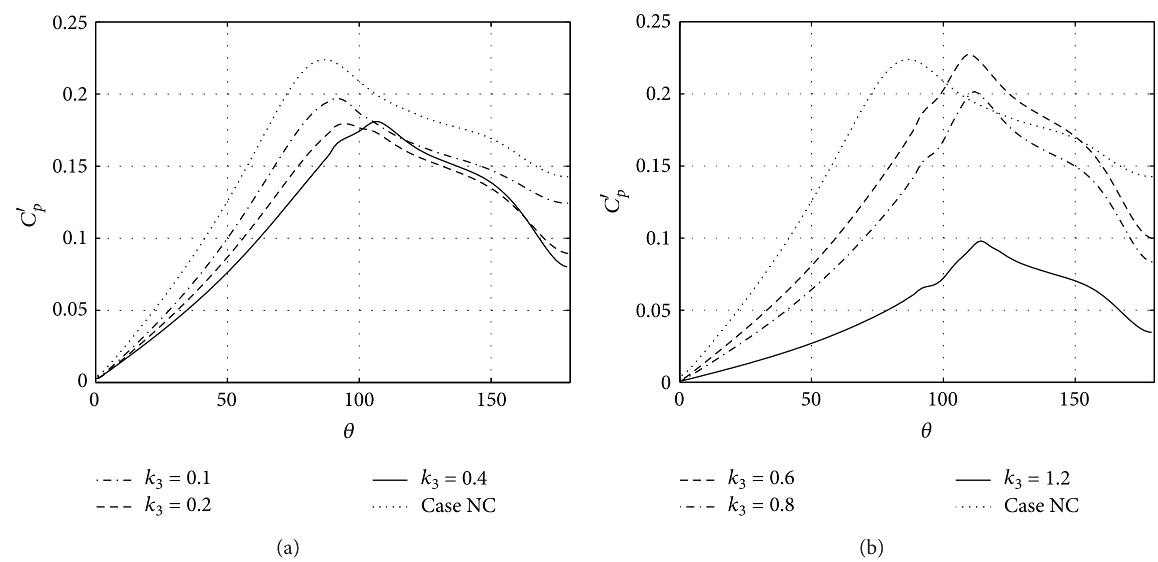

FIGURE 13: Distribution of pressure fluctuations C_p' on the cylinder surface in Case 1: (a) k_3 = 0.1, 0.2, and 0.4; (b) k_3 = 0.6, 0.8, and 1.2.

rates are obtained in $0.2 \leq k_3 \leq 0.6$, that is, 34% for drag and 96% for lift fluctuations.

The significant reduction in the mean drag and the lift fluctuations can be explained by the distribution of the pressure coefficient, C_p, and the RMS pressure coefficient, C_p', as shown in Figure 19. The shape of the pressure distribution on Position 1 is similar to that in Case 1, while that on Position 2 is similar to that in Case NC. On both Positions 1 and 2, however, the pressure in the rear half is higher than that in Case 1. This is considered due to the enhanced mixing of momentum by the three-dimensional forcing. The pressure fluctuations are much less than those in Case NC and Case 1 due to the three-dimensionalization (i.e., desynchronization) of vortex shedding; thus, the lift fluctuations are significantly decreased.

4. Conclusions

We have performed direct numerical simulation of a flow around a circular cylinder at the Reynolds number of Re_D = 1000 controlled using plasma actuators. A two-dimensional

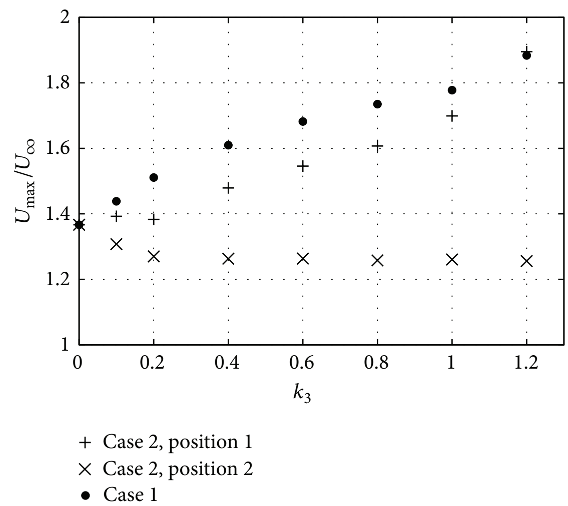

FIGURE 14: Maximum mean streamwise velocity around plasma actuator (upper surface on the cylinder; Position 2) for different forcing amplitudes (k_3) in Case 2.

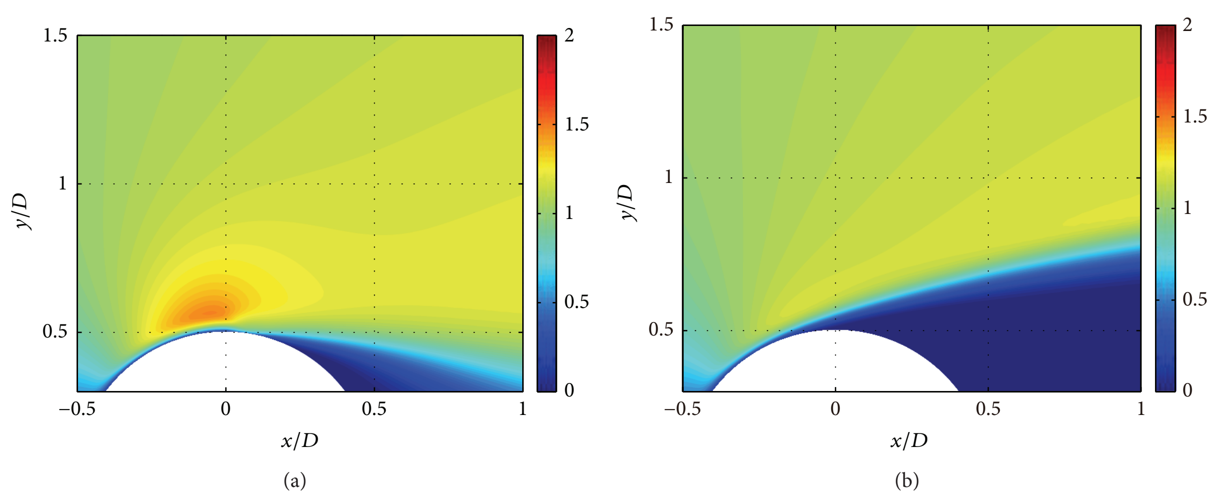

FIGURE 15: Mean streamwise velocity around the upper plasma actuator in Case 2 (k_3 = 0.4): (a) Position 1; (b) Position 2.

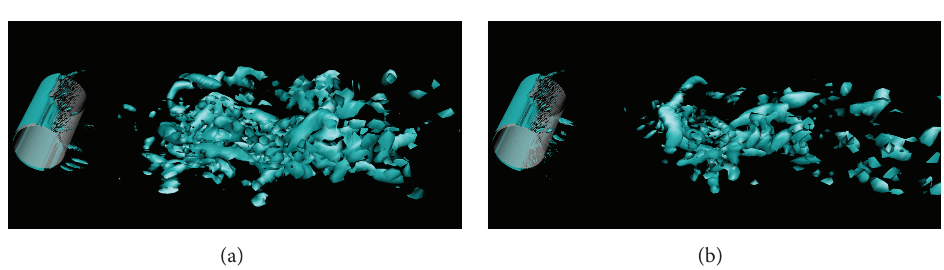

FIGURE 16: Instantaneous vortical structure in Cases 2 and 3 (k_3 = 0.4) identified by isosurfaces of $\|\Omega\|^2 - \|S\|^2$ = 1.0: (a) Case 2; (b) Case 3.

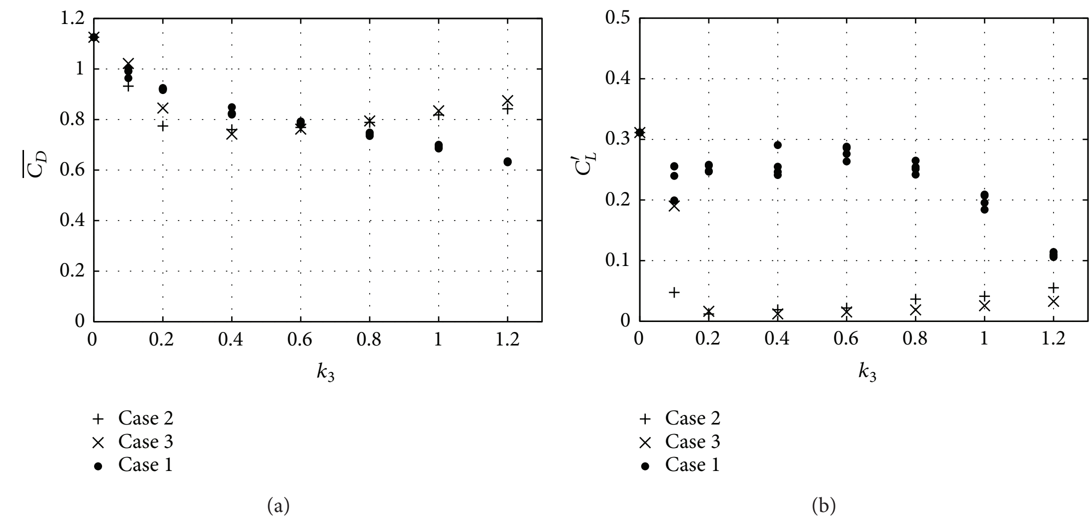

Figure 17: Mean drag and the RMS lift fluctuations for different forcing amplitudes (k_3) in Cases 2 and 3: (a) mean drag, $\overline{C_D}$; (b) RMS lift fluctuations, C_L'.

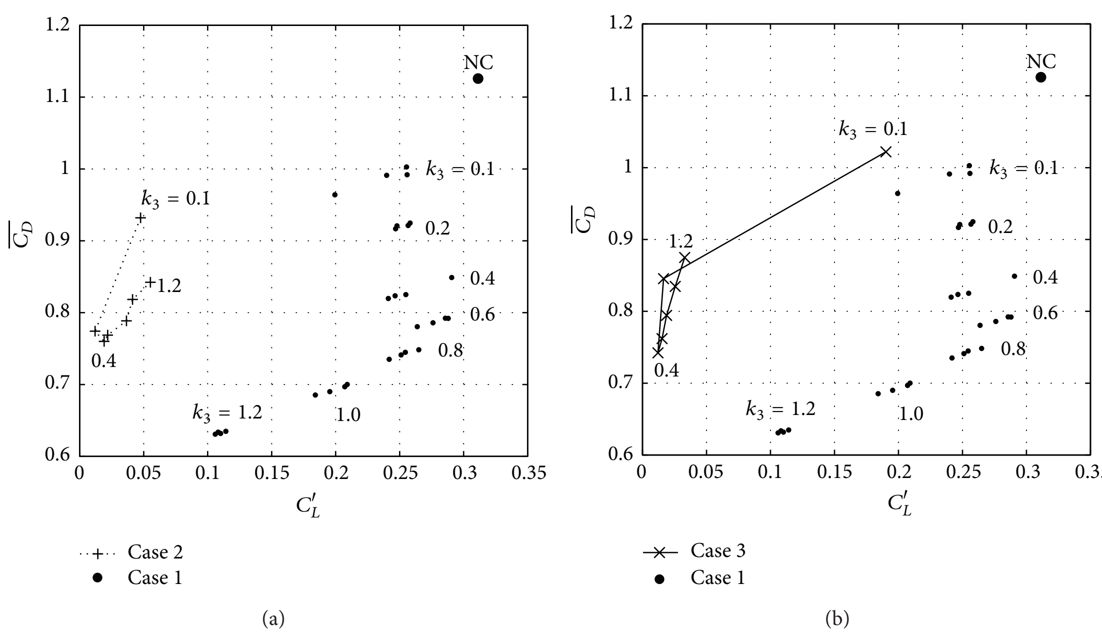

Figure 18: Relationship between C_L' and $\overline{C_D}$: (a) Case 2; (b) Case 3.

forcing and two types of three-dimensional forcing have been examined with different values of forcing amplitude.

In the two-dimensional forcing, higher forcing amplitude of the plasma actuators results in larger reduction of both the mean drag coefficient ($\overline{C_D}$) and the RMS lift coefficient (C_L'). In the best case, $\overline{C_D}$ and C_L' are reduced by 44% and 66%, respectively. The mechanism for these reductions is a direct feeding of mean momentum into the boundary layer, which delays the separation; thus, the pressure recovers on the rear surface and the vortex shedding is weakened.

On the other hand, the three-dimensional forcing is found to work well too. Regardless of the forcing amplitude, greater effects are obtained in the suppression of lift fluctuations compared to the case of two-dimensional forcing. Moreover, the drag is reduced as much as that in the two-dimensional forcing case, even at lower forcing amplitudes. In the best case, $\overline{C_D}$ and C_L' are reduced by 34% and 96%, respectively. The mechanism is found to be different from that for the two-dimensional forcing. The reduction of the mean drag and the lift fluctuations is due to three-dimensionalizaton of vortex shedding, which enhances mixing of momentum and desynchronizes the phase of vortex shedding.

In the present study, the total length of plasma actuators in the three-dimensional forcing is half of that in the

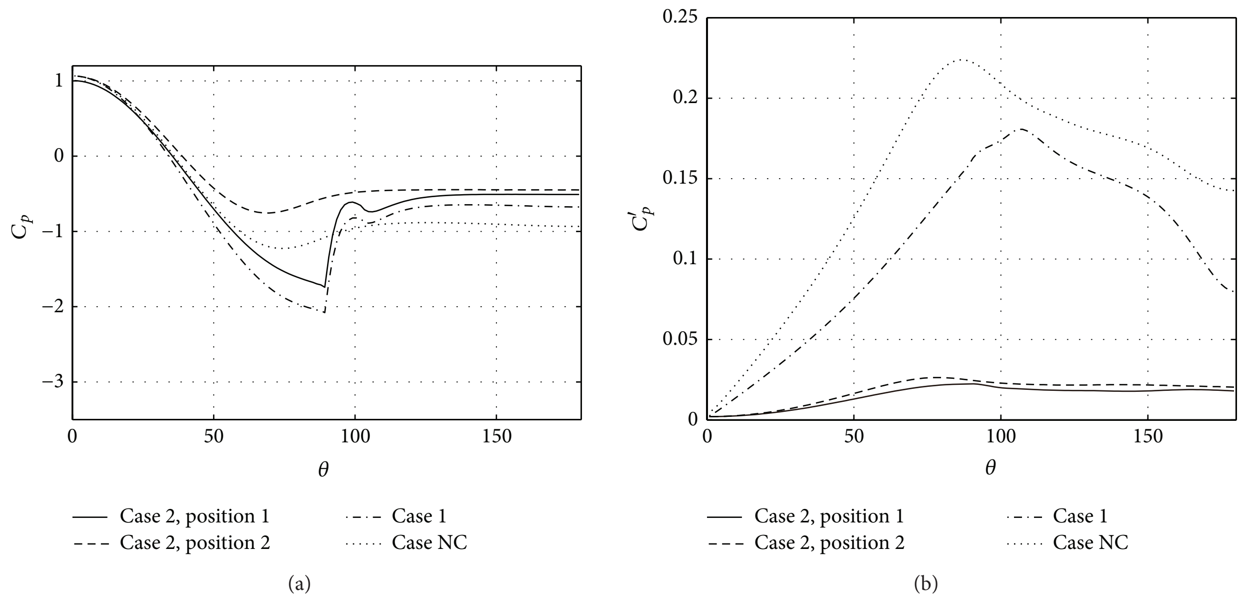

Figure 19: Distribution on the cylinder surface in Case 2 ($k_3 = 0.4$): (a) C_p; (b) C_p'.

two-dimensional forcing. Therefore, considering the power required for the present three-dimensional forcing, which is also nearly half of that for the two-dimensional forcing, the three-dimensional forcing is considered nearly twice more efficient than the two-dimensional forcing.

Of course, validity of the present findings is limited to the case of $\mathrm{Re}_D = 1000$. Although a similar effect may be expected at moderately high Reynolds numbers, the amounts of drag reduction and lift suppression should be significantly dependent on the Reynolds number. Moreover, the situation may drastically change around and above the critical Reynolds number ($\mathrm{Re}_D \sim 10^5$). Toward practical applications, a comprehensive study on the Reynolds number dependency should be conducted as a future work.

Conflict of Interests

The authors declare that there is no conflict of interests regarding the publication of this paper.

Acknowledgments

The authors are grateful to Drs. Shinnosuke Obi and Keita Ando (Keio University) for fruitful discussion. Koji Fukagata also thanks Ms. Arisa Chuma (Keio University) for assistance in artwork. This work was partly supported through Grant-in-Aid for Scientific Research (C) (no. 25420129) by Japan Society for the Promotion of Science (JSPS).

References

[1] H. Choi, W.-P. Jeon, and J. Kim, “Control of flow over a bluff body,” *Annual Review of Fluid Mechanics*, vol. 40, pp. 113–139, 2008.

[2] K. Kwon and H. Choi, “Control of laminar vortex shedding behind a circular cylinder using splitter plates,” *Physics of Fluids*, vol. 8, article 479, 1996.

[3] J. Choi, W.-P. Jeon, and H. Choi, “Mechanism of drag reduction by dimples on a sphere,” *Physics of Fluids*, vol. 18, Article ID 041702, 2006.

[4] H. Park, D. Lee, W.-P. Jeon et al., “Drag reduction in flow over a two-dimensional bluff body with a blunt trailing edge using a new passive device,” *Journal of Fluid Mechanics*, vol. 563, pp. 389–414, 2006.

[5] P. W. Bearman and J. C. Owen, “Reduction of bluff-body drag and suppression of vortex shedding by the introduction of wavy separation lines,” *Journal of Fluids and Structures*, vol. 12, no. 1, pp. 123–130, 1998.

[6] L. N. Cattafesta and M. Sheplak, “Actuators for active flow control,” *Annual Review of Fluid Mechanics*, vol. 43, pp. 247–272, 2011.

[7] J. Kim and H. Choi, “Distributed forcing of flow over a circular cylinder,” *Physics of Fluids*, vol. 17, Article ID 033103, 2005.

[8] J. R. Roth and X. Dai, “Optimization of the aerodynamic plasma actuator as an electrohydrodynamic (EHD) electrical device,” in *Proceedings of the 44th AIAA Aerospace Sciences Meeting and Exhibit*, Reno, Nev, USA, January 2006, AlAA 2006–1203.

[9] T. C. Corke, C. L. Enloe, and S. P. Wilkinson, “Dielectric barrier discharge plasma actuators for flow control,” *Annual Review of Fluid Mechanics*, vol. 42, pp. 505–529, 2010.

[10] S. Grundmann, S. Klumpp, and C. Tropea, “Stabilizing a laminar boundary-layer using plasma-actuators,” in *Proceedings of the 25th International Congress of the Aeronautical Science*, p. 255, Hamburg, Germany, September 2006.

[11] Y.-C. Cho and W. Shyy, “Adaptive flow control of low-Reynolds number aerodynamics using dielectric barrier discharge actuator,” *Progress in Aerospace Sciences*, vol. 47, no. 7, pp. 495–521, 2011.

[12] A. V. Kozlov and F. O. Thomas, “Bluff-body flow control via two types of dielectric barrier discharge plasma actuation,” *AIAA Journal*, vol. 49, no. 9, pp. 1919–1931, 2011.

[13] S. Bhattacharya and J. W. Gregory, "Effect of three-dimensional plasma actuation on the wake of a circular cylinder," in *Proceedings of the 50th AIAA Aerospace Sciences Meeting Including the New Horizons Forum and Aerospace Exposition*, Nashville, Tenn, USA, January 2012, AlAA 2012-0907.

[14] H. Naito and K. Fukagata, "Numerical simulation of flow around a circular cylinder having porous surface," *Physics of Fluids*, vol. 24, Article ID 117102, 2012.

[15] W. Shyy, B. Jayaraman, and A. Andersson, "Modeling of glow discharge-induced fluid dynamics," *Journal of Applied Physics*, vol. 92, no. 11, pp. 6434–6443, 2002.

[16] K. Fukagata and N. Kasagi, "Highly energy-conservative finite difference method for the cylindrical coordinate system," *Journal of Computational Physics*, vol. 181, no. 2, pp. 478–498, 2002.

[17] A. A. Wray, "Minimal storage time-advancement schemes for spectral methods," Tech. Rep. MS202 A-1, NASA Ames Research Center, 1990, unpublished.

[18] P. R. Spalart, R. D. Moser, and M. M. Rogers, "Spectral methods for the navier-stokes equations with one infinite and two periodic directions," *Journal of Computational Physics*, vol. 96, no. 2, pp. 297–324, 1991.

[19] J. K. Dukowicz, "Approximate factorization as a high order splitting for the implicit incompressible flow equations," *Journal of Computational Physics*, vol. 102, no. 2, pp. 336–347, 1992.

[20] S. Yamamoto and K. Fukagata, "Numerical simulation of a plasma actuator based on ion transport," *Journal of Applied Physics*, vol. 113, Article ID 243302, 2013.

[21] K. Inoue, *PIV measurement of separation control of flow around a circular cylinder using plasma actuator [M.S. thesis]*, Keio University, Tokyo, Japan, 2011.